A Low-Cost 60-GHz Modular Front-End Design for Channel Sounding

Muhammad Umar, Martin Laabs, Niels Neumann, and Dirk Plettemeier, *Member, IEEE*

***Abstract*— Millimeter-wave (mmWave) frequency bands are attractive for bandwidth (BW)-intensive applications. However, scholarly articles revealing straightforward and repeatable modular construction of mmWave front ends are scarce. Channel sounding, which is critical due to the distinct propagation characteristics of mmWaves, is predominantly done through bulky and expensive laboratory equipment due to the lack of other hardware. This work fills this gap through a modular approach to construct a 60-GHz front-end transceiver by packaging off-the-shelf chipsets and custom-designed blocks. In contrast to the typical expensive manufacturing processes for mmWave circuits, this work reports passive mmWave blocks, which are compatible with single-layer standard printed circuit board (PCB) process along with the measurement setup. Multilayer PCB stack-up is then used for system integration offering an economic and repeatable manufacturing. Distinguishing features of the developed front end are round-trip (half-duplex) communication, carrier reconfigurability within 58–64 GHz, and agent-mode operation. The front end is usable as a portable frequency-domain channel sounder. To the best of the authors' knowledge, it is the first report of a portable channel sounder, which can acquire a round-trip amplitude–frequency response of an mmWave channel without using any bulky or expensive laboratory equipment. This work further identifies the electromagnetic (EM) compatibility issues in unshielded PCBs and hardware response calibration. Furthermore, it identifies the hardware requirements to maintain channel reciprocity in round-trip communication at mmWave bands.**

***Index Terms*— Channel sounder, millimeter-wave (mmWave) printed circuit board (PCB), modular front end, PCB balun, planar-to-coaxial transition.**

I. Introduction

MODERN semiconductor device technology and electronic packaging solutions make millimeter-wave (mmWave) bands feasible for commercial deployment. An unlicensed band at 60 GHz is particularly attractive for short-range applications due to high free-space path loss and specific absorption. It has attracted industry and academia due to higher commercialization possibilities, as the band offers several gigahertz of continuous bandwidth (BW) throughout the globe, as summarized in Fig. 1. Solutions for channel models, waveforms, access control, and network protocols are being proposed, which need endorsement through implementation and characterization in a real wireless environment [1].

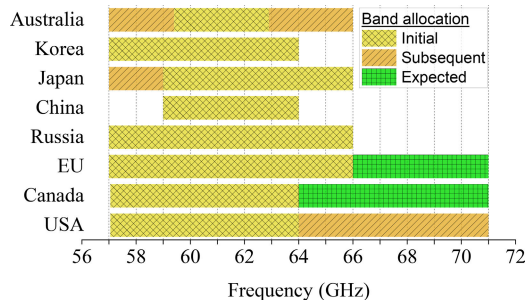

Fig. 1. 60-GHz unlicensed band allocations in various regions.

Contemporary research in the 60-GHz band shows a high dependence on commercially available off-the-shelf (COTS) front ends (e.g., [2], [3], [4], [5], [6], [7], [8], [9], [10], [11], [12], [13], [14]). However, COTS offers are limited, and the majority of the referred research has depended on a single manufacturer. COTS front ends provide a rapid solution; however, they have several technical limitations, such as simplex (one-way) communication, fixed frequency carriers, fixed frequency-synthesizer parameters, and noncompatibility for agent-mode operation in a system [15], [16]. Simplex platforms are a showstopper for roundtrip communication, and limited carrier frequencies do not support sweep and chirp applications, e.g., frequency-domain channel sounding (FCS). The provided user interface (UI) lacks self-automation or agent mode, e.g., for channel adapted modulation and coding. A survey indicates that the variety of off-the-shelf mmWave front ends is insufficient for state-of-the-art research activities [17].

On the other hand, scholarly articles revealing the modular construction of a standalone mmWave front end using semiconductor chipsets are also limited and lack the specifications mentioned above [18], [19], [20]. Chipset's integration into mmWave circuits requires application-specific redesigning of

Manuscript received 28 July 2023; revised 9 November 2023 and 20 December 2023; accepted 31 December 2023. Date of publication 12 January 2024; date of current version 11 March 2024. This work was supported by the German Federal Ministry of Education and Research (BMBF) through the Project "fast secure" within the framework of the Zwanzig20 Program under Grant 03ZZ0522B. Recommended for publication by Associate Editor X. Gu upon evaluation of reviewers' comments. *(Corresponding author: Muhammad Umar.)*

Muhammad Umar is with the Barkhausen-Institut gGmbH, 01067 Dresden, Germany (e-mail: muhammad.umar@barkhauseninstitut.org).

Martin Laabs and Dirk Plettemeier are with the Chair of RF and Photonics Engineering, Technische Universität Dresden, 01069 Dresden, Germany (e-mail: martin.laabs@tu-dresden.de; dirk.plettemeier@tu-dresden.de).

Niels Neumann is with the Institute of Electrical Information Technology, Technische Universität Clausthal, 38678 Clausthal-Zellerfeld, Germany (e-mail: niels.neumann@tu-clausthal.de).

Color versions of one or more figures in this article are available at https://doi.org/10.1109/TCPMT.2024.3353332.

Digital Object Identifier 10.1109/TCPMT.2024.3353332

passive components. Packaging involves electrically enlarged components, high-frequency interconnect parasitics, and increased susceptibility to manufacturing tolerances. Hence, modular construction of mmWave front-end board involves significant work compared with legacy microwave bands' front ends. Working toward in this direction, Umar et al. [21], [22], [23], [24] have already contributed several essential blocks and interconnects.

Wave propagation in millimeter and beyond-mmWave bands shows distinctive characteristics in each scenario calling for channel sounding, accomplishable either in time or in frequency domain [25], [26]. Time-domain channel sounding involves impulse, spread spectrum, or orthogonal frequency division multiplexing waveforms requiring high peak-to-average power ratios, dynamic range, and complex hardware [27], [28]. On the other hand, FCS (aka vector network analyzer (VNA)-based sounding) utilizes frequency sweeps covering large BWs with relatively simple hardware. However, it takes relatively longer to acquire the channel response but is still useful for static or slow varying channels [29]. Time-domain characteristics, e.g., power delay profile, multipath resolution, and unambiguous time range, are calculated from frequency-dependent path loss information using signal processing techniques [30], [31]. The state-of-the-art reported setups for mmWave FCS are dependent on bulky and expensive laboratory equipment justifying a need for handy and low-cost hardware [32], [33], [34], [35], [36], [37], [38].

This article reports a modular design of 60-GHz front end by packaging COTS components with custom-designed components. Passive mmWave blocks (balun, coaxial-to-planar, and waveguide launcher) are reported, all functional on at least 15% fractional BW and compatible with low-cost printed circuit technology (PCT). The front end supports half-duplex mode and allows carrier-frequency selection with sub-MHz resolution, quadrature modulation, and output power control. A valuable feature is its autonomous and agent-mode operation enabling algorithm-based applications. The front end is useable for digital data communication and as a bidirectional (forward and reverse channel) FCS for measuring amplitude–frequency response of the channel without involving any laboratory equipment, which is, to the best of the authors' knowledge, yet new to be reported in standalone mmWave front ends. The printed circuit board (PCB) compatible design allows easier application-specific upgradation, supporting the research culture. Section II of this article discusses the design criteria and technology choice. Section III introduces the building blocks, followed by their integration in Section IV. Section V presents the system characterization, while utilization of the front end as a channel sounder is given in Section VI.

II. Design Criteria and Technology

This design targets 10% fractional BW at 60 GHz, i.e., 58–64 GHz covering the majority of allocation standards, as given in Fig. 1. The important parameters for FCS are multipath resolution τ_{res} and unambiguous time range τ_{unamb}, calculated from the frequency-domain information as follows [36]:

$$\tau_{\text{res}} = \frac{1}{\text{BW}_s} \quad \text{and} \quad \tau_{\text{unamb}} = \frac{1}{f_{\text{res}}} \tag{1}$$

where BW_s is swept BW with frequency step resolution f_{res}. Published channel sounding campaigns report an unambiguous-time range of 200 ns providing a reliable indoor channel characterization [36]. It corresponds to a maximum frequency step of 5 MHz using (1). A detachable antenna is opted, facilitating laboratory characterization of the front-end and antenna-related experiments. At V-band, RF connectivity for the antenna requires 1.85-mm precision coaxial connector or WR-15 waveguide standard. Similarly, the digital connectivity to the front end is essential, providing reconfigurability and agent-mode operations (under the control of an external processor). Digital connectivity is provided through a universal serial bus and a universal asynchronous receiver transmitter (UART) port. A comparison summary of front-end features is given in Table I.

TABLE I
Availability of the Proposed Features in 60-GHz Front Ends

Feature	COTS		Scholarly articles			This work
	[15]	[16]	[18]	[19]	[20]	
Tx/Rx mode	Sx.	Sx.	Sx.	Sx.	Sx.	H.Dx.
BW (GHz)	57–64	57–64	57–64	60–63	58–64	58–64
Carrier step f_{res} (MHz)	500	500	500	Fixed carrier	Fixed carrier	1
Freq. sweep	✗	✗	✗	✗	✗	✓
Fix antenna	✗	✗	✓	✗	✗	✗
Agent mode	✗	✗	✓	✗	✗	✓
User interf.	GUI	GUI	✗	✗	✗	CMD

Sx.: simplex H.Dx.: half duplex
GUI:graphical user interface CMD: Command line user interface

The choice of transceiver chipset is essential, as its application-specific utilization requires additional off-the-shelf and new custom-made components. HMC6000 series by Hittite and BGT chipset family offered by Infineon Technologies cover the targeted 58–64-GHz band [39], [40]. Both comprise inbuilt mixers, oscillator, low noise amplifier, and power amplifier. Infineon BGT chipset is selected in this work for its advantages of duplex operation and external frequency synthesizer over HMC6000 series. However, the downside is its differential RF and IF interfaces requiring conversion to single-ended 50 Ω for our application. The block diagram of the front-end design is given in Fig. 2. This work presents the design and integration of the required off-chip 60-GHz components.

This work utilizes multilayer PCT for its low cost and rapid prototyping. However, mmWave circuits on PCT need additional attention due to the lower layout resolution and process accuracy compared with thin- and thick-film processes. An order of under/overetching is usually unavoidable in standard PCT processes, as shown in an example structure in Fig. 3(a), manufactured through a commercial pooling offer.

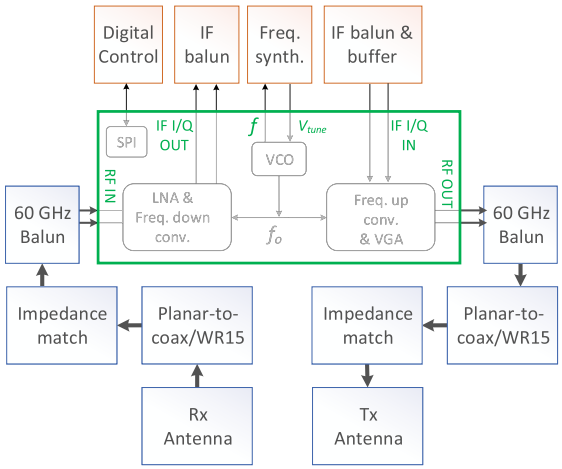

Fig. 2. Block diagram of the proposed front end. The block with border shows the COTS mmWave chipset.

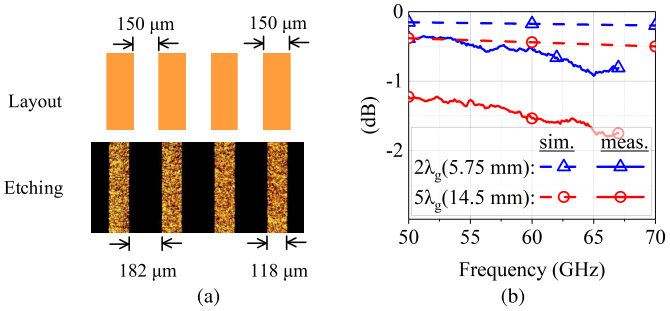

Fig. 3. (a) PCB layout dimensions in comparison with its manufactured sample. (b) Signal attenuation in 50-Ω matched microstrips.

TABLE II
DIELECTRIC SUBSTRATE PROPERTIES AND PCB PROCESS RESOLUTION

Substrate		Process	
Dielectric constant	3.66	Line & gap resolution	0.1 mm
Loss tangent	0.0087	Min. via diameter	0.1 mm
Copper thickness	35 µm	Min. via pitch	0.35 mm
Dielectric height	254 µm	Min. via pad diameter	0.3 mm

Further challenges include frequency dependence of substrate parameters, e.g., dielectric constant (ϵ_r) and loss tangent (tan$D$). They are usually available for a reference frequency much lower than mmWave bands, and their frequency dependence may result in resonance shifts and increased insertion loss at the actual frequency of operation. An example is plotted in Fig. 3(b) for the substrate Isola I-Tera MT, showing that the measured loss is higher than the original simulation performed using vendor-provided substrate parameters referred at 10 GHz, i.e., $\epsilon_r = 3.45$ and tan$D = 0.0031$ [41]. This substrate has been experimentally analyzed for operation at a range of mmWave frequencies in [42], providing the effective values of ϵ_r and tan$D$. The experimentally determined properties of Isola I-Tera MT at 60 GHz in [42] (given in Table II) have been used in this work to achieve an agreement between simulations and measurements.

III. BUILDING BLOCKS

A. Balun

A conventional coupled line balun requires 30 μm of coupling gaps when optimized at 60 GHz for the chosen substrate, which is unrealizable with PCT. Similarly, N-section half-wave and log-periodic baluns are also unpractical due to parasitic coupling between the adjacent sections due to reduced section size at mmWave frequencies. In this work, we utilize Marchand balun with "double-edge coupling" technique presented by Umar et al. [21], [22]. The planar Marchand balun configuration is popular for its simplicity. In this configuration, an open-circuited half-wavelength line couples two oppositely phased signals into a pair of short-circuited quarter-wavelength lines. To compensate for the wide coupling gaps on PCB, we utilize two pairs of quarter-wavelength lines on both edges of the half-wavelength line as notable in the layout of the balun given in Fig. 4(a). Both pairs are then connected using bond wires. The overall impedance of the lines is increased to match the bondwires' impedance, and the port impedances are tuned using microstrip tapers. Fig. 4(a) shows the design layout. The balun is optimized for 58–64-GHz BW in contrast to [21] targeting 50–67 GHz. Fig. 4(b) and (c) presents the simulated response of the balun compared with the previous design. The 1.8 dB of amplitude mismatch at 59 GHz has been reduced to 1 dB, while input return loss remains better than 10 dB for 58–64 GHz.

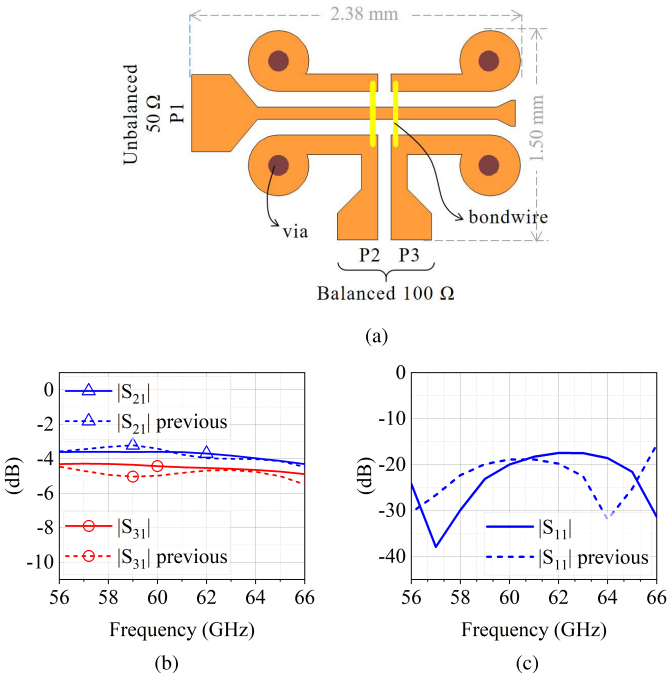

Fig. 4. Improved double-edge coupled Marchand balun. (a) Layout. (b) and (c) simulation results compared with [21]—(b) insertion loss and (c) return loss.

Two baluns are manufactured as connected back-to-back with their differential ports for laboratory measurements. It avoids differential probing and eases the measurement setup and calibration. The measured response is then compared with the simulated response of the same back-to-back connected configuration. Standard PCB manufacturing offers 100 μm of trace-to-trace clearance; however, minimum coupling gaps of 115 μm are used in this design. It is to avoid working on the technological limits and to tolerate a level of etching

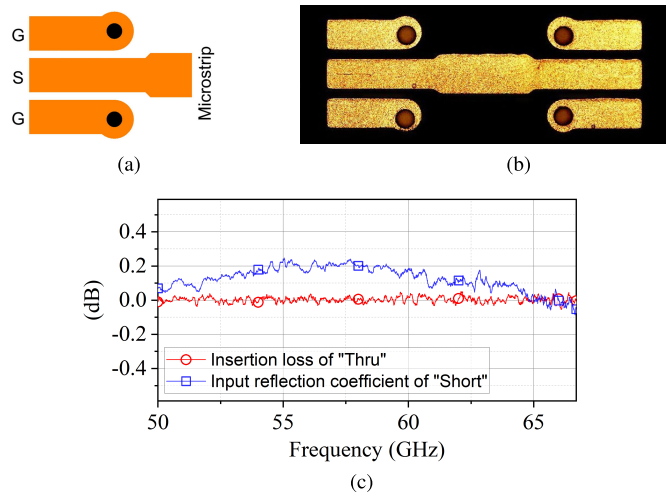

Fig. 5. GSG probing. (a) Launch pad. (b) Photograph of the "thru." (c) Calibration verification results.

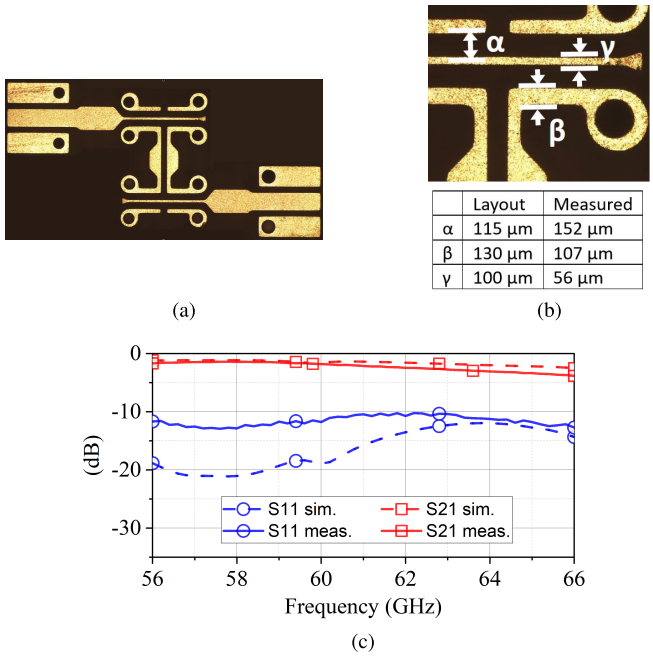

Fig. 6. Back-to-back connected Marchand balun. (a) Manufactured prototype. (b) Layout measurements. (c) Simulation and measurement results.

inaccuracies, in contrast to [21] where simulation and measurements could not match due to process tolerance. Similarly, via holes are enlarged from 100 to 150 μm, and via pads are increased to 450 μm easing the drilling process. As the balun exploits bond wires for connectivity, the bond-wire profile needs particular attention at mmWave frequencies [24]. The design is bonded through 25-μm gold wires using a semiautomatic TPT-HB16 bonder (in [21], a manual bonder K&S-4500-Series was used).

Measurements are obtained through a laboratory setup comprising Rohde & Schwarz ZVA67 VNA, 400-μm pitch ground–signal–ground (GSG) probes from GGB Inc., and a manual probe station from MPI Corporation. Since the design is a microstrip structure, a probe launch pad is designed, which interfaces the GSG probe to the microstrip, given in Fig. 5(a). The test fixture is removed through two-port thru–reflect–line (TRL) calibration standards designed on the same used substrate. Two back-to-back connected probe lunch pads are used as "thru" [Fig. 5(b)], an open-ended launch pad produces "reflect," and two launch pads connected through a length provide "line." The calibration process removes the fixture loss (cables, probes, and launch pad) and brings the reference plane to the center of back-to-back connected launch pads (the "thru"). It is verified by postcalibration reprobing of the "thru" and "reflect"; the measured insertion loss and reflection coefficient are plotted in Fig. 5(c), showing a maximum deviation of 0.2 dB from the ideal value of 0 dB. The VNA supports a frequency range of up to 67 GHz.

The prototype of the balun is manufactured along with probe launch pads, given in Fig. 6(a). The measurement results are plotted in Fig. 6(c). It can be noticed that measurement (solid lines) follows the simulation (dash lines) curve trend, however, with reduced input matching and slightly higher insertion loss. This deviation arises, as the process tolerance becomes significant to the wavelength at mmWave frequencies. Umar et al. [21], [23] have analyzed this phenomenon by modeling the etching errors in the simulation software. Fig. 6(b) shows mismatches between manufactured and original layout dimensions. Nevertheless, measurements show 10-dB input impedance matching throughout the desired BW, confirming the balun application in the front end.

By comparing the design process and measurement results with [21], it is deduced that mmWave circuits on PCT require careful manufacturing; a tolerance margin in the design is preferable. Bond-wire loop profiles can affect the performance of mmWave circuits. Fortunately, state-of-the-art automatic and semiautomatic wire bonders can realize precalculated profiles with high repeatability. Removal of the test fixture is also important to obtain the true response of the device under test (DUT). Off-the-shelf calibration substrates remove the cable and probe fixture from measurements bringing the reference plane to the probe tips. However fixture present on the PCB, e.g., the launch pad in our case, still comes as a fixture. In contrast, on-substrate calibration standards can shift the measurement reference plane to the actual DUT ports.

B. Planar-to-Coaxial Transition

A planar-to-coaxial transmission line transition provides connectivity to a detachable antenna or characterization equipment. Rosenberger 08K80A-40ML5 precision connectors can provide this transition for up to 70 GHz. However, they introduce an impedance mismatch if directly attached to the top of a planar transmission line. When pressed against a microstrip on the PCB, the connector's body accompanies the microstrip from both sides creating a coplanar waveguide (CPW) environment. Hence, a smooth microstrip-to-CPW transition is required to avoid impedance mismatch. The coaxial part of the connector is elevated 30° from the PCB with the inner conductor touching the feedline and two-sided metallic body touches the ground pad. It is modeled here like a GSG RF probe touching a launch pad on a substrate. For launch pads, the GSG probe response is eliminated from the

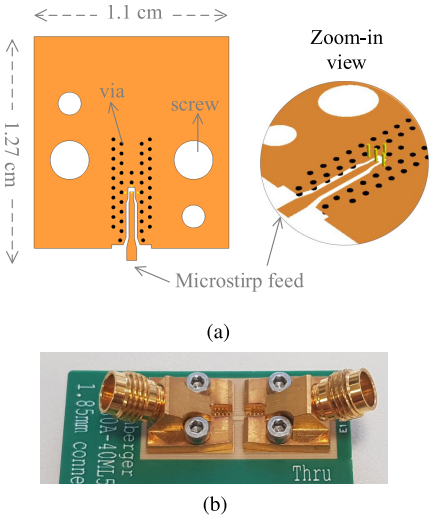

Fig. 7. Coxial connector. (a) Launch-pad layout. (b) Manufactured in back-to-back configuration for measurement.

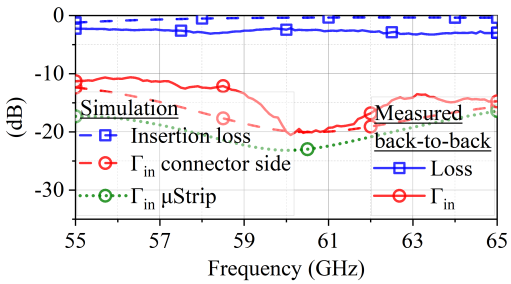

Fig. 8. Simulation and measured results for planar-to-coaxial conversion.

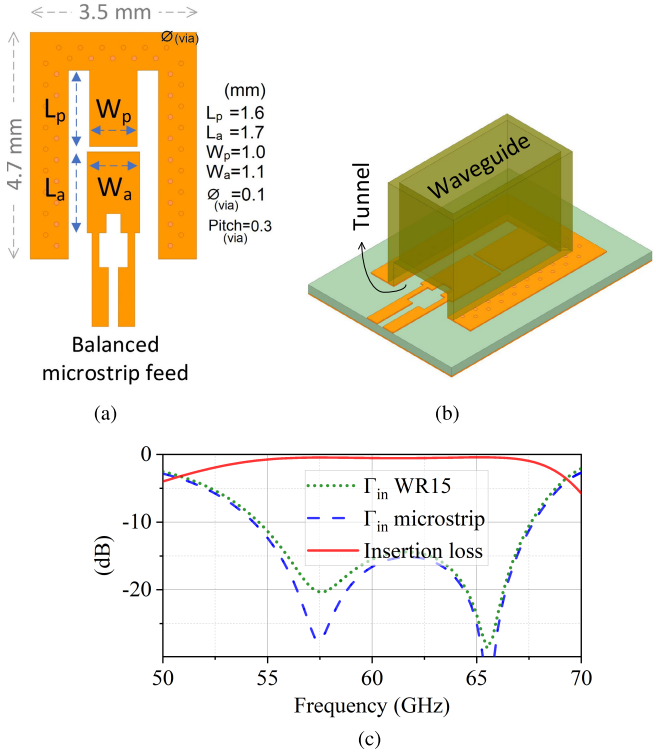

Fig. 9. Differential-microstrip-to-WR15 waveguide conversion structure. (a) Footprint. (b) Flange placement. (c) Simulation results.

results through a calibration processes; however, this transition needs attention, because the effect cannot be calibrated out; instead, it remains a part of the system.

The scenario is simulated in a 3-D electromagnetic (EM) simulator (AWR microwave office) as a combination of microstrip-to-CPW transition followed by CPW-to-GSG probe transition. Tapers minimize the impedance mismatch at signal-carrying conductors and both side-ground planes providing a smooth microstrip-to-CPW transition, as shown in the layout in Fig. 7(a). Signal-line-to-ground spacing is kept compatible with the PCB process. A via grid connects the top and bottom ground plane for ground stability. A minimum via diameter of 100 μm and pitch of 350 μm is ensured to guarantee standard PCB process compatibility. The footprint for the connector is optimized for insertion loss and input return loss at both sides, i.e., microstrip and probe end, using the EM simulator.

Dash curves in Fig. 8 show the simulation results for the planar-to-coax conversion with insertion loss curve and return loss curves for both sides as input. For simplicity reasons, a prototype is manufactured with two such structures connected back-to-back with their microstrip sides, as visible in the photograph in Fig. 7(b). This reduces the measurement setup complexity. The measured results for a back-to-back assembly are also plotted in Fig. 8 with solid curves. The measured insertion loss is 2.5 dB at the center frequency for the back-to-back assembly, and half-insertion loss is expectable from a single structure. The measured return loss is better than 10 dB for 55–65 GHz.

C. Planar-to-Waveguide Transition

In the case of providing waveguide connectivity, a direct differential-microstrip-to-WR15 transition would be helpful eliminating the balun. A popular technique is short-ended cavity resonators on the back side of the PCB [43], [44], [45]. However, our simulations for a multilayer stack show that reflections on each prepreg-core boundary of the sandwiched PCB contribute to the signal attenuation. Other approaches use U-shaped or nonuniform ridge flanges requiring complex manufacturing [46], [47]. One approach is radiating the signal inside the waveguide by a planar antenna on a thin (127 μm) substrate [48], [49]. An extension of this technique is performed in this work by implementation on a multilayer stack having a thick prepreg substrate while keeping the layout resolution compatible with standard PCT.

The design comprises of a differential feedline exciting a planar patch inside the waveguide with a parasitic patch coupled to the active patch through a narrow coupling gap. The layout of this structure is shown in Fig. 9(a). This approach can achieve two matched resonance frequencies by tuning both patches to different frequencies. Wave leakage into the prepreg substrate is a challenge in this type of design. Leakage is eliminated in the original proposed design in [49] through a dense via fence; however, the via diameter and pitch dimensions are undisclosed. In this work, drill holes with a minimum pitch of 0.3 mm are possible with the selected

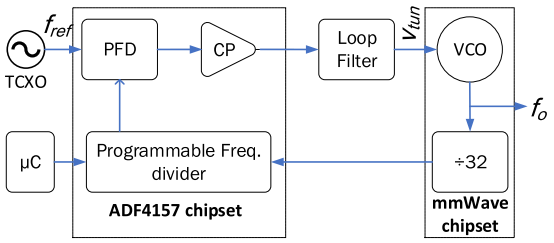

Fig. 10. Block diagram of the designed frequency synthesizer.

PCT; hence, a second layer of via is introduced, resulting in a zig-zag via fence to mitigate leakage. A waveguide flange with a feedline tunnel is attached to the PCB in a way shown in Fig. 9(b). The size of the tunnel opening is optimized for a trade-off between energy leakage versus feedline-to-waveguide body coupling. The upper internal plane of the PCB stack-up is used to develop a uniform ground plane right under the via fence, separating the core and lower prepreg of the stack-up. Improved BW response is achieved for a relatively thick substrate. Optimization using a 3-D EM simulator (Ansys HFSS) shows 21% relative BW compared with 17% in [49]. Fig. 9(c) shows 10-dB matched input from 55 to 67 GHz on microstrip and waveguide ports with insertion loss <0.5 dB.

The planar-to-waveguide design is concluded here with simulation results. Manufacturing is not performed as in the author's laboratory, and the equipment is mainly available in coaxial technology. This design, however, is helpful for the interested research groups in the repetition and upgradation of the front end. Authors suggest an interesting economical way of its prototyping as 3-D printed plastic waveguide flange, metal plated through a silver-mirror-test process [50].

D. Frequency Synthesizer

The built-in voltage-controlled local oscillator (VCO) of the used mmWave transceiver chipset requires a tuning voltage v_{tune}, which is generated through a phase lock loop (PLL). The chipset has local oscillator (LO) tunable range of 57–64 GHz and provides 32-times frequency-divided LO output bringing the synthesizer operation down to 1.78–2.0 GHz. Fig. 10 shows a block diagram of the frequency synthesizer. The PLL's phase-frequency detector (PFD) and frequency divider are provided by Analog Devices ADF4157 chipset programmable through serial peripheral interface (SPI) interface [51]. Its acceptable input frequency range (from VCO) is 0.5–6 GHz, and maximum phase detector frequency is 32 MHz. The loop simulation is performed using ADISimPLL software with ADF4157 chipset model, 20-MHz reference oscillator, a passive third-order loop filter, and an ideal VCO with gain equal to the built-in VCO of the mmWave chipset. Simulation results for phase noise and settling time for a maximum frequency step are given in Fig. 11(a) and (b), respectively, for three different loop BWs. Fig. 11 shows a trade-off between phase noise and frequency settling time for given loop BWs.

The frequency synthesizer prototype is manufactured on a four-layer PCB with an onboard temperature-compensated reference oscillator. A photograph is given in Fig. 12. An onboard

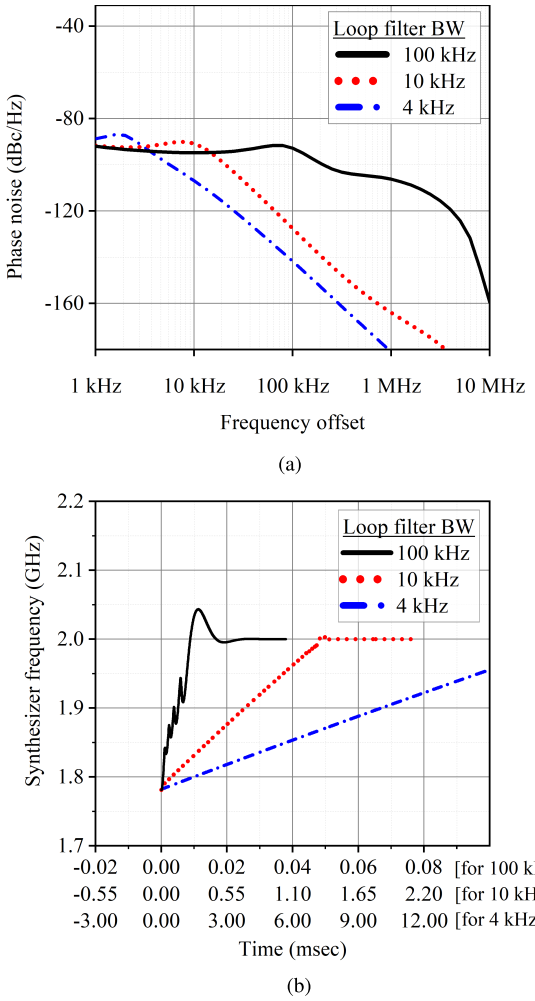

Fig. 11. Simulation results for PLL considering an ideal VCO. (a) Phase noise. (b) Settling time (218.75-MHz step), each curve plotted for its respective time scale for clarity of curve trend.

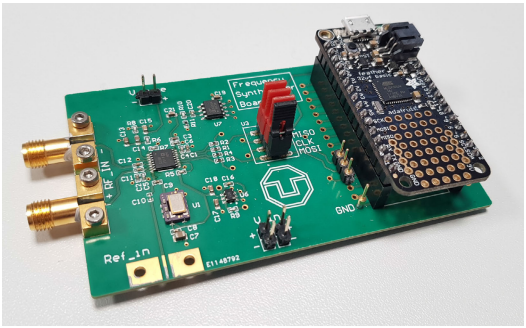

Fig. 12. Developed frequency synthesizer circuit.

microcontroller provides a UI for frequency input and performs SPI read/write operations. Before interfacing with the transceiver chipset, the synthesizer operation is verified using a COTS VCO "CVCO55CW" from Crystek Microwaves with operational frequency range of 1550–2500 MHz [52]. The measured voltage-to-frequency relationship and phase noise are verified with the datasheet. Phase noise curve is given in Fig. 13 measured with Rohde & Schwarz FSW67 spectrum analyzer (SA). The measured phase noise curve

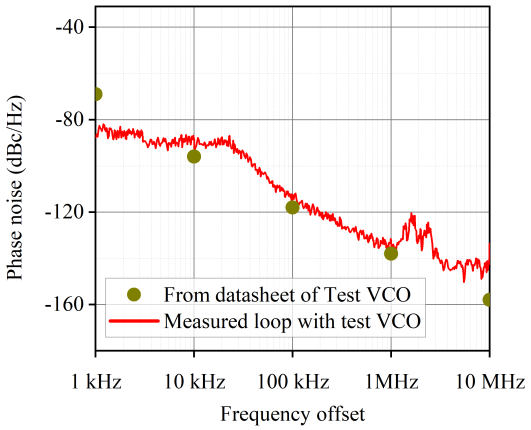

Fig. 13. Measured results for PLL with 10-kHz loop and test VCO.

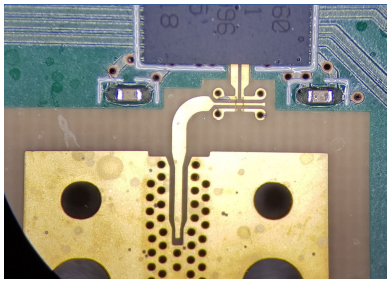

Fig. 14. Zoomed-in view of the RF board.

shows an overall slight increased phase noise, compared with the simulated in Fig. 11(a), as it contains both VCO and PFD noise. Sharp peaks are noticed at 1500- and 2500-kHz offset originating from the switching mode power supply. Manufacturer-provided phase noise of the test VCO is also plotted on the given frequency points. At 1-kHz offset, VCO performs better in the loop compared with free-running values given in the datasheet.

IV. System Integration and UI

The integration is accomplished on a four-layer PCB stack-up, 0.25-mm-thick Isola I-Tera MT as prepreg and 0.5-mm FR4 as a core. The top metal layer is used for RF and IF routing, and bottom layer carries digital and VCO-tune signaling. Internal two layers act as power planes and provide isolation between the upper and bottom layer signaling to avoid crosstalk.

The utilized mmWave transceiver chipset provides its electrical connectivity through a ball grid array (BGA) configuration with ball bumps' diameter 200 μm and pitch 500 μm. Its RF and IF I/Q ports support differential signaling only. Two 60-GHz baluns (from Section III-A) are placed near its RF pads to minimize microstrip loss, however ensuring an adequate distance for wire bonder capillary for the wire bonding process of the balun, as noticeable from the microscopic photograph in Fig. 14. Wire bonder HB-16 from TPT is used with 25-μm gold wire for wire bonding. The planar-to-coaxial transition structures (from Section III-B) are connected to the single-ended port of each balun. Afterward, Rosenberger 08K80A-40ML5 connectors are mounted on the pads, which

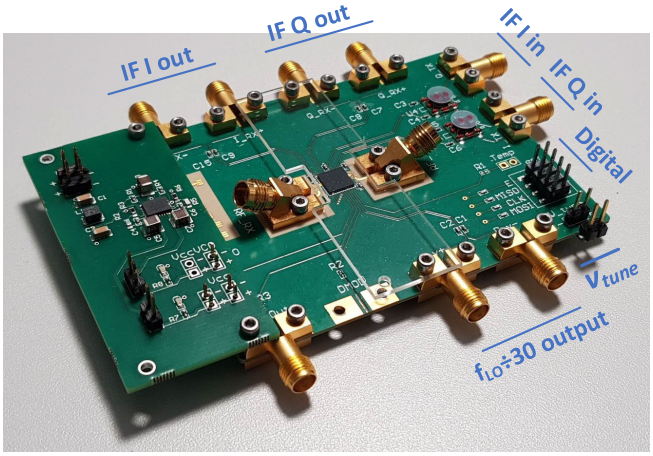

Fig. 15. Photograph of manufactured RF board.

act as Tx and Rx coaxial RF ports. Since the transceiver chipset supports only the differential signals on its 100-Ω IF interface for the transmitter chain, surface mount devices (SMD) baluns (MABA-CT2010) from Macom have been used to provide standard single-ended 50-Ω connectivity to the front end. The photograph of the developed RF board is shown in Fig. 15. A buffer circuit is separately designed to amplify and match IF outputs from the receiver chain. It comprises an impedance matching network and Texas Instruments THS4509q1 differential operational amplifier for each I and Q line, followed by surface mount technology (SMT) baluns for differential to single-ended conversion.

The front end is realized in three modules: RF board, receiver-buffer board, and frequency-synthesizer board connected through coaxial and ribbon cables. A separate module for each operation provides individual circuit characterization and easy troubleshooting. The drawback is that long board-to-board interconnects can cause signal integrity and EM interference (EMI) problems (as follows in Section V). In addition, it results in a relatively larger prototype size; however, it is acceptable as a first prototype in our case. A miniaturized version on a single PCB is, of course, possible in the future.

An SPI network is set up to access the internal registers of PFD and transceiver chipsets. A single-master dual-slave SPI network is developed using an ATmega32u4 microcontroller clocked at 8 MHz as master while PFD and transceiver chipsets as slaves. System parameters' reconfiguration, such as carrier frequency, output power level, switching Tx/Rx chain on/off, I/Q modulation enable/disable, and modulator current calibration, is possible by accessing the microcontroller through its universal serial bus. Furthermore, agent mode is supported through UART port of the microcontroller. All three devices in this SPI network share clock, master-in slave-out (MISO), and master-out slave-in (MOSI) signals, while chip enable (CS) for both slave chipsets is kept separate. The 10-Ω resistors are used in the SPI bus for an optimized line termination suppressing overshoot in long ribbon cables. The network is tested by writing predefined register values and reading back. At 1 Mb/s, a bit error rate (BER) of $<10^{-4}$ has been verified.

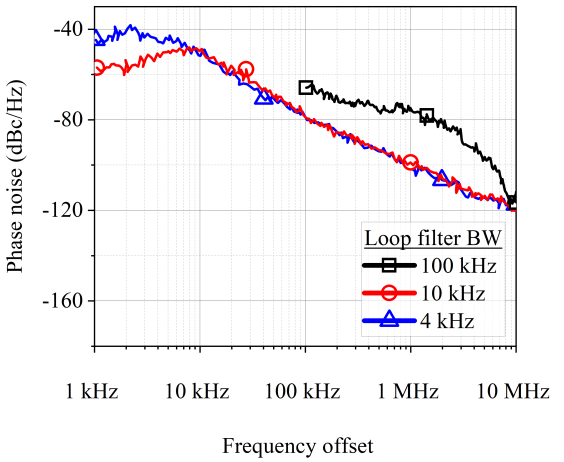

(a)

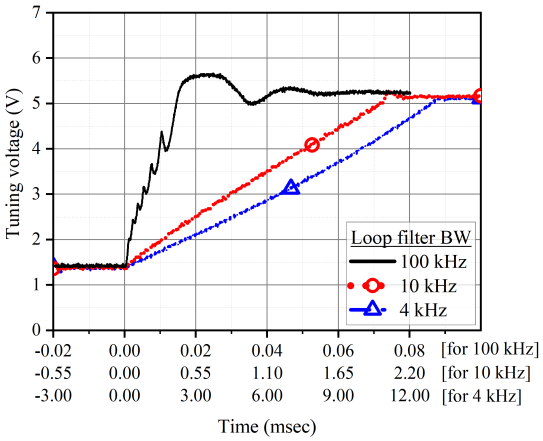

(b)

Fig. 16. Measured LO (a) phase noise at 60 GHz and (b) settling time for 7-GHz frequency step for varied loop BW.

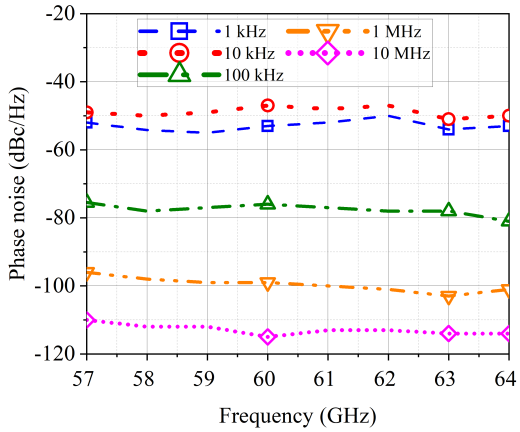

Fig. 17. Measured phase noise for 10-kHz loop BW and various carrier frequencies.

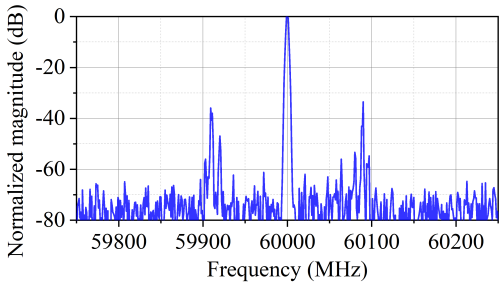

Fig. 18. Output spectrum with free running LO at 60 GHz, acquired with SA resolution BW of 3 MHz.

V. Characterization

A. Local Oscillator

The inbuilt VCO of the transceiver chipset is operated with our designed frequency synthesizer. The phase noise is measured through Rohde & Schwarz FSW67 SA for various loop BWs, given in Fig. 16(a). Unlike the simulation results in Fig. 11(a), the phase noise for 4- and 10-kHz loop filter BW is almost equal, showing a dominant VCO-generated noise, although the difference is notable for a loop BW of 100 kHz where PFD noise is very high below 100-kHz offset. Due to the high noise level, a measurement could not be carried out below 100-kHz offset from the carrier, as the SA could not fix on the carrier frequency. The settling time for a frequency shift of 7 GHz (from 57 to 64 GHz) is given in Fig. 16(b) for the same loop BWs acquired by a digital oscilloscope. The 100-kHz loop BW results in the fastest locking, although with cycle slips. Comparing Fig. 16(a) and (b) for phase noise and settling time, 10-kHz loop BW can be a good choice, offering low phase noise and still acceptable settling time. For 10-kHz loop BW, phase noise for various carriers between 58 and 64 GHz is measured by varying the LO frequency of the front end through the UI, as shown in Fig. 17. Phase noise of less than -95 dBc/Hz is noted at 1-MHz offset from the carrier for all frequencies. The off-chip passive loop filter is reconfigurable through replacing SMD components according to the intended application, e.g., faster lock times for frequency hopping or lower phase noise for high data rate transmission.

The output of the transmitter chain at 60 GHz without applying any IF input is plotted in Fig. 18. LO output peak is visible at 60 GHz, while two extra peaks appear at ± 90 MHz from the carrier. They appear due to EMI in the unshielded ribbon cable, which carries v_{tune} signal from the frequency synthesizer board to the RF board. This phenomenon has been verified by replacing the ribbon with a coaxial cable in the second development iteration of the front end for a different project. Nevertheless, the magnitude of these noise peaks is below 30 dB on the normalized magnitude scale.

B. Transmitter

An absolute maximum input power level of 0 dBm and a recommended maximum frequency of 500 MHz are applicable for each IF input imposed by the chipset in use. Carrier suppression is possible by adjusting the modulator current through UI, and sideband suppression is possible by adjusting the IF I-to-Q signal phase. An upconverted signal spectrum for 60-GHz LO and 500-MHz IF is shown in Fig. 19. Carrier (LO) and lower sideband (LSB; LO $-$ IF) suppression of more than 20 dB is achieved by the modulator current and I/Q-phase calibration on the cost of a harmonic component appearing at LO + 2IF. However, the second harmonic is also 20 dB below the desired upper sideband (USB) peak.

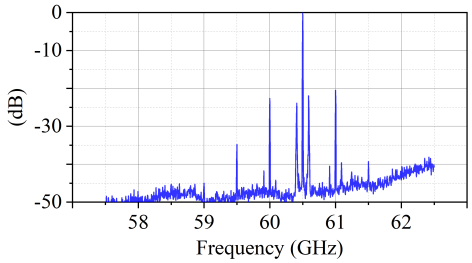

Fig. 19. Upconverted signal spectrum for 500-MHz IF, acquired by SA resolution BW 3 MHz and normalized to 0 dBm.

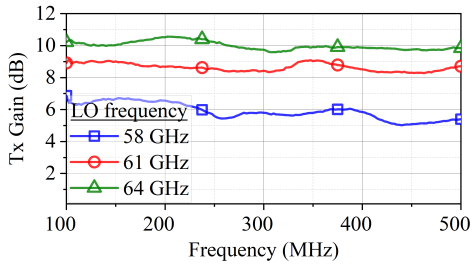

Fig. 20. Measured transmitter gain with sliding IF and fixed LO for minimum, center, and maximum LO frequencies, acquired by VNA.

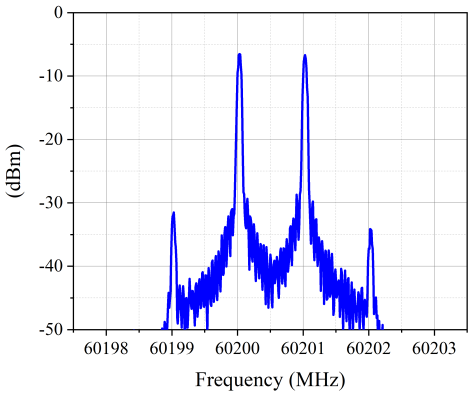

Fig. 21. Output spectrum for intermodulation products measurement.

Transmitter gain measurement has been performed by Rohde & Schwarz ZVA67 VNA. The VNA generates and slides the input IF-signal frequency while measuring the output RF power generated by the Tx chain at 60-GHz band. The front end generates LO internally, and the process is repeated for several LO frequencies. The measured transmitter gain is noted to be almost constant against IF variation, as plotted in Fig. 20, and cable losses have been taken into account.

The same VNA is used for intermodulation measurements. Two closely spaced frequencies, 200 and 201 MHz, are generated at two ports of the VNA. Both signals are combined through a power combiner and fed to the front end for upconversion. The third port of the VNA measures the upconverted RF signal, while LO is generated by the front end internally. Two desired peaks appear in the USB spectrum at $f_{\mathrm{LO}} +$ 200 and $f_{\mathrm{LO}}+201$ MHz, while the third-order intermodulation products appear at $f_{\mathrm{LO}} + 199$ and $f_{\mathrm{LO}} + 202$ MHz. After compensating for the cable losses, the spectrum for 60-GHz LO frequency is plotted in Fig. 21.

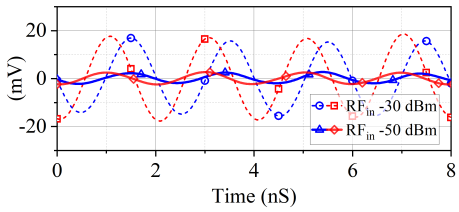

Fig. 22. Downconverted signal waveforms using 60-GHz LO frequency for RF input frequency 60 500 MHz, acquired by digital oscilloscope.

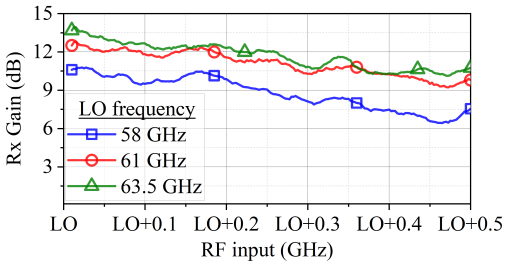

Fig. 23. Measured receiver gain with sliding IF and fixed LO for minimum, center, and maximum LO frequencies, acquired by VNA.

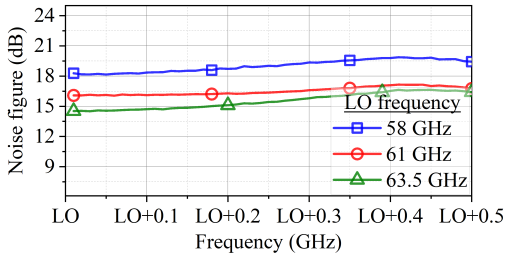

Fig. 24. Measured receiver noise figure.

C. Receiver

The transceiver chipset imposes an absolute maximum RF input power of 0 dBm and recommended maximum signal BW of 500 MHz for its RF receiver port. Downconversion result of exemplary RF signal at 60 500 MHz through LO setting of 60 GHz is given in Fig. 22. A corresponding IF signal at IF = RF − LO is generated for each RF input.

Receiver chain gain is measured by the same procedure adopted for transmitter gain measurement. VNA generates RF on one of its ports and measures the downconverted IF on the other. LO is generated internally by the front end using a frequency synthesizer and in-build VCO controlled through the UI. Receiver gain curves for the minimum, center, and maximum LO frequencies are plotted in Fig. 23. A decrease in gain versus the IF frequency is noticed in the measured results.

The Y-factor method is employed for front-end's receiver noise figure characterization. A V-band calibrated noise source Noisecom NC5115 and an FSW67 SA are used for measurement. A low-frequency noise source Noisecom NC346KA is used for the second-stage calibration of the measurement setup. Curves plotted in Fig. 24 present the double sideband noise figure of the receiver for swept IF and LO at band edges and center.

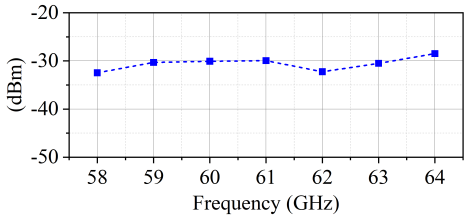

Fig. 25. LO leakage from Rx port out.

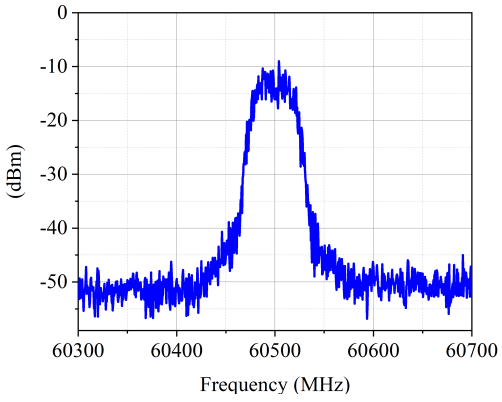

(a)

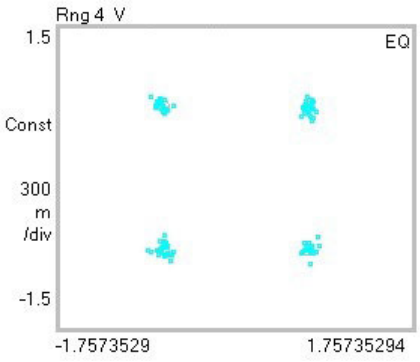

(b)

Fig. 26. (a) Spectrum and (b) I/Q constellation of the QPSK signal generated through Tx chain.

The same SA is used to measure LO leakage through the receiver RF port. LO is swept in steps through UI to characterize leakage power, which is plotted in Fig. 25.

VI. Application Example I: Communication System

The designed front end is utilized in transmission and reception of digital data at 60 GHz. For transmitter application, Anritsu 3710A vector signal generator (VSG) is used to generate I and Q baseband waveforms from pseudorandom bit sequences. Through the operational limits imposed by the VSG, a maximum data rate of 50 Mb/s can be generated per channel with raised cosine filtering and upsampling factor of 3. Furthermore, the VSG mixes the baseband to a nonzero carrier frequency. Hence, both baseband waveforms are obtained centered at 500-MHz frequency and applied at I and Q IF inputs of the designed front end. With the front-end LO frequency of 60 GHz, the output spectrum of a quadrature phase shift keying (QPSK) signal carrying a total of 100 Mb/s data rate is shown in Fig. 26(a) captured by SA. The acquired QPSK signal at 60 GHz has been analyzed by a digital signal analyzer (DSA). Since a V-band DSA is not available at the authors' laboratory, a high-fidelity downconversion of the RF signal to 2-GHz carrier is performed using Rohde & Schwarz FSW67 SA. Then, Agilent DSA90804A DSA supported by Agilent 89600VSA software is utilized for extracting the I/Q constellation, presented in Fig. 26(b). The DSA extracts a quadrature error of 1.39° and error vector magnitude (EVM) of 7.3% rms.

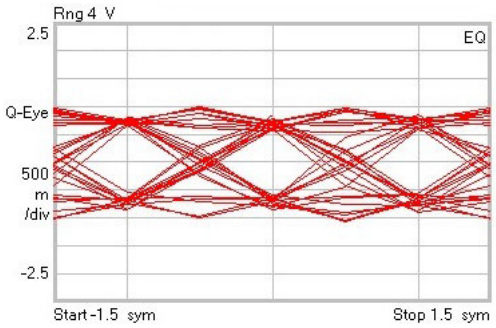

Fig. 27. Eye diagram from the Rx-chain output.

The same 60-GHz QPSK modulated signal is used to demonstrate receiver application. Due to unavailability of 60-GHz VSG in the authors' laboratory, one unit of the developed front end is used as transmitter, and a second unit is used to downconvert the 100-Mb/s QPSK signal from 60-GHz to 500-MHz IF, which DSA then analyzes. Automatic clock recovery and equalization algorithms of the DSA provide eye diagrams for I and Q components. The eye diagram of only one component is presented here as a sample in Fig. 27. An EVM of 10.4% rms and signal-to-noise ratio (SNR) 19.6 dB is calculated by the DSA for complete transmitter–receiver setup.

VII. Application Example II: Channel Sounder

The features of carrier reconfiguration and agent-mode operation enable the front end to be used for FCS, aka VNA sounding. A complete channel response consists of amplitude and phase information; however, in the current implementation, we extract channel amplitude response only to keep the signal processing simple. Half-duplex (forward channel and then reverse channel) sounding is made possible at 60 GHz using two units of the developed front ends. For baseband processing and units' synchronization, Redpitaya STEMlab 125-14 is used, which is an economical COTS digital signal processor kit [53]. It supports digital connectivity through UART and Ethernet. It provides two fast-analog inputs and two outputs supporting frequencies up to 50 MHz on each, with analog-to-digital (ADC) and digital-to-analog (DAC) sampling rate of 125 MS/s.

A. Synchronization

Redpitaya STEMlab is used as a master controlling two RF-front-end units as agents through UART and transmitting

commands on a simplex link without handshake protocol. The sounding setup is simplified using wired synchronizaiton of both front ends; however, it limits the sounding distance. For longer distance channel characterization, alternative approaches have been used in the state-of-the-art channel sounders, e.g., using optical fiber link in [37] and Rubidium clock in [54]. Redpitaya maintains Tx–Rx synchronization by sending 16-bit UART commands simultaneously to both units containing information about next frequency point and each unit's operation as Tx or Rx. Implemented resolution of frequency sweep is 1 MHz (fulfilling indoor channel requirements at 60 GHz, see Section II). However, resolution beyond 1 MHz is also possible by the developed front-end units.

B. Sweep Generation, Downconversion, and Data Processing

Two 90° out-of-phase 20-MHz tones are generated through Redpitaya and used as IF I and Q inputs for the front-end units; 20 MHz for IF is chosen, because laboratory experiments revealed Redpitaya DAC and ADC have better voltage accuracy at this frequency, which is almost the center of its operating BW. LO frequency of each front end is kept 20 MHz below the transmission frequency, so that USB can be used after upconversion at the correct frequency, i.e., $f_{\mathrm{LO}}+20$ MHz. LSB suppression is necessary, because it acts as an image frequency at the same frequency offset from the receiver LO as USB. It is possible downconversion to the same IF that can add a channel response, which is 40 MHz away from the desired frequency. LSB suppression is achieved by phase tuning of the baseband I and Q tones through the Redpitaya source code. LSB and carrier suppression have already been shown in Section V-B.

Programming Redpitaya to send UART commands, increasing the LO in defined frequency steps initiates LO sweep. Fig. 28 shows a spectrum with frequency sweep step 10 MHz with 2-ms dwell time on each frequency point. Within the dwell time, the channel sounder completes a round trip channel measurement for that particular frequency point. Only a portion of the total BW is shown with relatively larger frequency step (10 MHz) for plot clarity. When received on the receiver unit, each carrier in the frequency sweep, synchronized through digital circuitry, gets downconverted back to 20-MHz IF carrying channel response of the carrier. The recovered IF is sampled by Redpitaya, and the power of the signal is calculated as follows:

$$P = \frac{1}{N}\sum_{n=1}^{N}|x(n)|^2 \tag{2}$$

where x is the sample value and N is the sample space size, 16 384 for Redpitaya. The calculated power is saved against the carrier frequency in CSV format by Redpitaya.

C. Assembly and Calibration

A single Redpitaya generates I and Q IF signals on its two fast-analog outputs. Power splitters provide each I and Q signal to both front-end units to avoid a second Redpitya unit in the system. However, only one front-end unit, working as Tx, uses the IF signals at a time. The receiver unit downconverts each received RF frequency to 20-MHz I and Q IF output. Since we are interested in the path loss only, either I or Q component of the receiver is used for processing, since both components bring the same channel path loss information. The use of both components can improve system sensitivity; however, an advanced DSP kit with four IF input channels could be used. Fig. 29 shows the channel sounder assembly. A Redpitaya is configured as controller, and two front-end units as agents on the UART bus.

Since each RF-chain block and RF channels of Redpitaya have a nonflat frequency response, the measured response will not be an accurate channel response. To calibrate the hardware, a coaxial cable is measured by connecting it between two units, i.e., the Tx port of one and Rx of the second front end, and sweeping frequency between 58 and 64 GHz. A calibrated VNA measures the same cable afterward, and an error curve is obtained, shown in Fig. 30. This curve shows the hardware response and is eliminated from channel measurement results. For operation in the wireless channel, the front-end

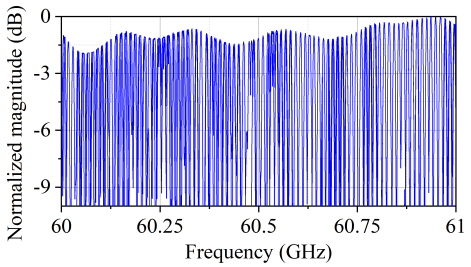

Fig. 28. Frequency sweep generated through Tx chain.

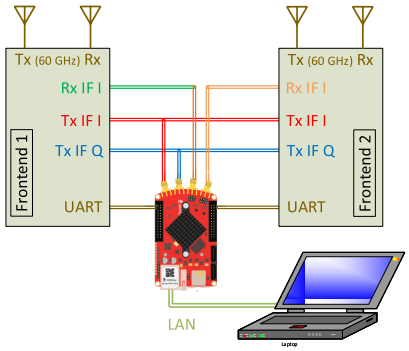

Fig. 29. Front-end units in channel sounder setup.

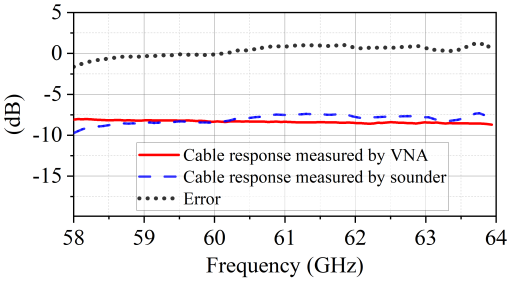

Fig. 30. Measured response of a coaxial cable by channel sounder and VNA.

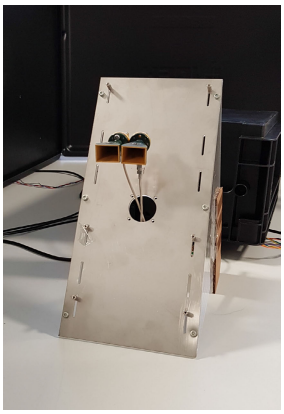

Fig. 31. Photograph of a front-end unit. Circuit boards are shielded in a metallic casing while Tx and Rx antenna extruding out.

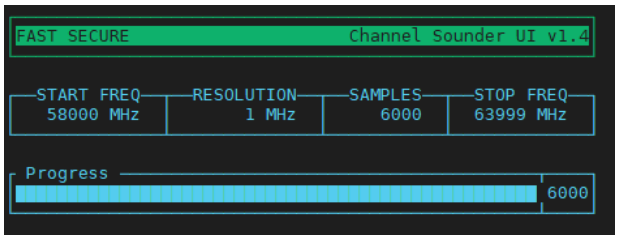

Fig. 32. Developed UI for channel sounder.

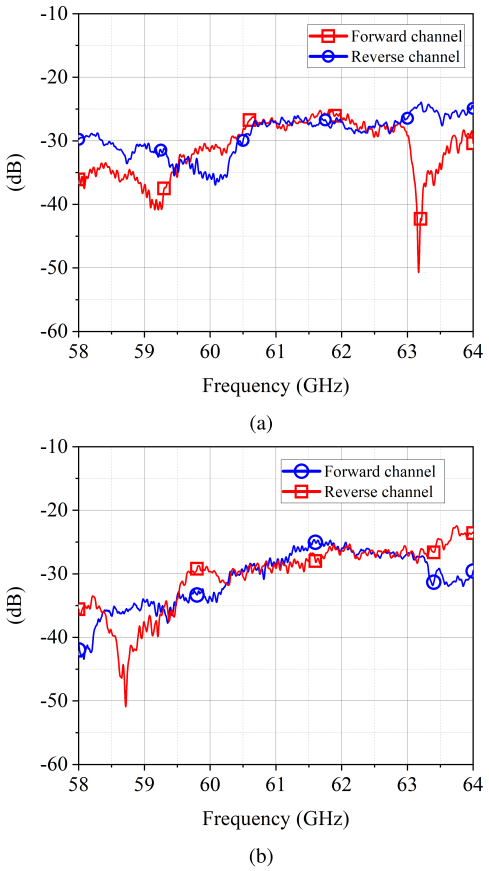

Fig. 33. Bidirectional channel sounding results in indoor environment. (a) Scenario 1. (b) Scenario 2.

units are equipped with COTS horn antennas SAR-2309-15-S2 from Sage Millimeter Inc. The frequency dependence of antenna gain impacts the acquired channel response. It is true even when using a calibrated VNA for swept frequency sounding. For an accurate channel response with significant frequency-dependent antenna gain, sounding equipment can be calibrated inside an anechoic chamber. However, it is not the case here as each antenna has a maximum gain fluctuation of 0.4 dBi between 58 and 64 GHz, as given in its datasheet, with 23-dBi gain at 60 GHz. Furthermore, EMI in the circuit boards can impact the results. It was observed that results deviate if the bare circuit board of the receiver front end comes in the line of sight to the transmitter antenna. To mitigate EMI, circuit boards of each front-end unit are enclosed in a metallic shielding with Tx and Rx antennas extruding out, as shown in Fig. 31.

D. Short-Distance Channel Sounding

A screenshot of the developed UI is shown in Fig. 32. User inputs start, stop, and sweep resolution. The frequency band between 58 and 64 GHz can be swept with a minimum frequency step size of 1 MHz. The system requires 3.75 W of continuous power during the sounding operation. Channel measurements are conducted in indoor environments. Multipath is introduced in the wireless channel by an assembly of Teflon rods between the two front-end units, and various channels were created by changing rods' positions. Tx-to-Rx distances of up to 5.5 m were possible, restricted by shared IF and UART cables connecting to a single Redpitaya. Fig. 33 presents two examples of bidirectional sounding results.

Despite forward and reverse calibration and having identical antenna model for both stations, a level of difference is notable between forward and reverse channel response. The reason for this mismatch is that each front-end unit is transmitting and receiving from its separate antennas. However, both antennas are placed close to each other (as visible in Fig. 31), but still center-to-center separation is $>\lambda/2$, because $\lambda = 5$ mm at 60 GHz in free space. It creates a difference in traveling routes for forward and backward propagating waves. Hence, they interact with different objects in the environment and experience dissimilar reflection and scattering. In contrast, if a VNA is used for sounding, the internal circulator at each port enables transmission and reception by the same antenna, forcing forward and backward traveling waves to follow the same path and preserving the channel reciprocity.

The bidirectional channel sounding results obtained from this study establish that antenna duplexing is required at each station in case a reciprocal channel is required for specific applications, e.g., channel reciprocity-based key generation in physical layer security. A comparison of state-of-the-art FCS setups is presented in Table III. The previously reported setups provide unidirectional sounding and do not support digital data communication. The hardware presented in this article is usable for channel adapted modulation and coding, i.e., measure first and then use optimal transmission parameters.

TABLE III
STATE-OF-THE-ART mmWAVE FCS SETUPS

Ref.	Bandwidth (GHz)		Resolution (MHz)	Tx/Rx sync.	Distance (m)	Calibration	Equipment/ Hardware	Sounding mode
[32]	35	[75 – 110]	N.A.	Wired	3.6	B2B	VNA+Extender	Simplex
[33]	20	[90 – 110]	3.3	Wired	2.25	B2B	VNA+Extender	Simplex
[54]	6	[58 – 64]	Chirp	Rubidium clock	38	Anechoic	Coaxial modular	Simplex
[34]	3.5	[60.5 – 64]	7	Wired	4.3	N.A.	VNA+Freq.synth	Simplex
[35]	2	[57 – 59]	2.5	Wired	12	Anechoic+B2B	VNA+Mixers	Simplex
[36]	1	[63.4 – 64.4]	0.625	Wired	50	Anechoic	VNA+Mixers	Simplex
[37]	1	[59.6 – 60.6]	0.1	Optical fibre	100	B2B	COTS modules+PXI	Simplex
This work	6	[58 – 64]	1	Wired	5.5	B2B	Planar & SMD modular	Half duplex

N.A.: not available. B2B: back-to-back. PXI: setup from National Instruments

VIII. CONCLUSION

Distinct propagation characteristics of each mmWave band call for channel sounding for link management. Due to the inadequate variety of hardware available for mmWave bands, frequency-domain channel sounders have been predominately reported using bulky laboratory equipment. This article simplifies this task through a modular 60-GHz transceiver front-end design. It involves packaging of available off-the-shelf chipsets along with custom-designed passive blocks, e.g., 60-GHz balun, planar-to-coaxial transition, and frequency synthesizer on economical PCT. This work addresses the challenges imposed by standard PCT on mmWave circuits, e.g., coarse layout resolution and process tolerances. The reported front end is operatable as transmitter or receiver on time-domain basis with a reconfigurable carrier frequency on the fly with in 58–64-GHz BW using the command line interface. The front end can be programed for operation in an algorithm or used in agent mode by an external processor, a feature not available in the existing designs. Two application examples of the hardware are demonstrated, i.e., digital data transmission/reception and FCS. Bidirectional channel sounding is demonstrated within 58–64 GHz with 1-MHz resolution without using any laboratory equipment in the setup. To the best of the author's knowledge, this work reports the first frequency-swept mmWave channel sounder, which sounds in both forward and reverse channels without using any laboratory equipment in the setup. Sounding results show a mismatch in forward and reverse channel path loss due to using separate antennas for the transmitter and receiver on each front-end unit. Results show that channel reciprocity at mmWave bands is achievable only if the hardware with an antenna duplexing solution is employed. This will be addressed in further studies. The developed front end is usable for channel adapted digital data transmission.

ACKNOWLEDGMENT

This work has been carried out in the Chair of RF and Photonics Engineering, TU Dresden, Dresden, Germany.

REFERENCES

[1] T. Nitsche, G. Bielsa, I. Tejado, A. Loch, and J. Widmer, "Boon and bane of 60 GHz networks," in *Proc. 11th ACM Conf. Emerg. Netw. Experiments Technol.*, New York, NY, USA, Dec. 2015, pp. 1–13, doi: 10.1145/2716281.2836102.

[2] A. Loch, A. Asadi, G. H. Sim, J. Widmer, and M. Hollick, "mm-Wave on wheels: Practical 60 GHz vehicular communication without beam training," in *Proc. COMSNETS*, Jan. 2017, pp. 1–8. [Online]. Available: http://ieeexplore.ieee.org/document/7945351/

[3] W. Khawaja, O. Ozdemir, and I. Guvenc, "UAV air-to-ground channel characterization for mmWave systems," in *Proc. IEEE 86th Veh. Technol. Conf. (VTC-Fall)*, Sep. 2017, pp. 1–5. [Online]. Available: http://ieeexplore.ieee.org/document/8288376/

[4] H. Boeglen, "A 60 GHz digital link with GNU radio and USRP radios," in *Proc. GNU Radio Conf.*, 2021, pp. 1–2.

[5] J. O. Lacruz, R. R. Ortiz, and J. Widmer, "A real-time experimentation platform for sub-6 GHz and millimeter-wave MIMO systems," in *Proc. 19th Annu. Int. Conf. Mobile Syst., Appl., Services*. New York, NY, USA: ACM, Jun. 2021, pp. 427–439, doi: 10.1145/3458864.3466868.

[6] A. Quadri, H. Zeng, and Y. T. Hou, "A real-time mmWave communication testbed with phase noise cancellation," in *Proc. IEEE INFOCOM Conf. Comput. Commun. Workshops*, Apr. 2019, pp. 455–460. [Online]. Available: https://ieeexplore.ieee.org/document/8845251/

[7] J. O. Nielsen, W. Fan, P. C. F. Eggers, and G. F. Pedersen, "A channel sounder for massive MIMO and mmWave channels," *IEEE Commun. Mag.*, vol. 56, no. 12, pp. 67–73, Dec. 2018. [Online]. Available: https://ieeexplore.ieee.org/document/8570042/

[8] J. Zhang, X. Zhang, P. Kulkarni, and P. Ramanathan, "OpenMili: A 60 GHz software radio platform with a reconfigurable phased-array antenna," in *Proc. Annu. Int. Conf. Mobile Comput. Netw.*, 2016, pp. 162–175.

[9] T. Wei and X. Zhang, "MTrack: High-precision passive tracking using millimeter wave radios," in *Proc. 21st Annu. Int. Conf. Mobile Comput. Netw.*, New York, NY, USA, Sep. 2015, pp. 117–129, doi: 10.1145/2789168.2790113.

[10] Y. Zeng, P. H. Pathak, Z. Yang, and P. Mohapatra, "Poster abstract: Human tracking and activity monitoring using 60 GHz mmWave," in *Proc. 15th ACM/IEEE Int. Conf. Inf. Process. Sensor Netw. (IPSN)*, Apr. 2016, pp. 1–2. [Online]. Available: http://ieeexplore.ieee.org/document/7460704/

[11] Y. Ghasempour, M. K. Haider, and E. W. Knightly, "Decoupling beam steering and user selection for MU-MIMO 60-GHz WLANs," *IEEE/ACM Trans. Netw.*, vol. 26, no. 5, pp. 2390–2403, Oct. 2018. [Online]. Available: https://ieeexplore.ieee.org/document/8457527/

[12] Y. Ghasempour and E. W. Knightly, "Decoupling beam steering and user selection for scaling multi-user 60 GHz WLANs," in *Proc. 18th ACM Int. Symp. Mobile Ad Hoc Netw. Comput.*, New York, NY, USA, Jul. 2017, pp. 1–10, doi: 10.1145/3084041.3084050.

[13] R. Foster et al., "Beam-steering performance of flat Luneburg lens at 60 GHz for future wireless communications," *Int. J. Antennas Propag.*, vol. 2017, pp. 1–8, Jan. 2017. [Online]. Available: https://www.hindawi.com/journals/ijap/2017/7932434/

[14] M. Kim, H. Kinh, Y. Chang, and J.-I. Takada, "Development of low-cost 60-GHz millimeter-wave MIMO channel sounding system," in *Proc. 6th Global Symp. Millim. Waves*, Sendai, Japan, 2013, pp. 18–21.

[15] *60 GHz Transmit/Receive (Tx/Rx) Development System*. Accessed: Mar. 2, 2023. [Online]. Available: https://www.pasternack.com/images/ProductPDF/PEM009-KIT.pdf

[16] *EK1HMC6350 User Guide—UG-1031—Analog Devices*. Accessed: Mar. 2, 2023. [Online]. Available: https://www.analog.com/media/en/technical-documentation/user-guides/ek1hmc6350-ug-1031.pdf

[17] R. Gomes et al., "Will COTS RF front-ends really cope with 5G requirements at mmWave?" *IEEE Access*, vol. 6, pp. 38745–38769, 2018.

[18] P. Zetterberg and R. Fardi, "Open source SDR frontend and measurements for 60-GHz wireless experimentation," *IEEE Access*, vol. 3, pp. 445–456, 2015.

[19] L. Duarte, R. Gomes, C. Ribeiro, and R. F. S. Caldeirinha, "A software-defined radio for future wireless communication systems at 60 GHz," *Electronics*, vol. 8, no. 12, p. 1490, Dec. 2019. [Online]. Available: https://www.mdpi.com/2079-9292/8/12/1490

[20] M. J. Horst, M. T. Ghasr, and R. Zoughi, "Design of a compact V-Band transceiver and antenna for millimeter-wave imaging systems," *IEEE Trans. Instrum. Meas.*, vol. 68, no. 11, pp. 4400–4411, Nov. 2019. [Online]. Available: https://ieeexplore.ieee.org/document/8613867/

[21] M. Umar, M. Laabs, N. Neumann, and D. Plettemeier, "60 GHz double edge coupled Marchand balun for PCB implementation," in *Proc. 49th Eur. Microw. Conf. (EuMC)*, Oct. 2019, pp. 332–335.

[22] M. Umar, M. Laabs, J. Damas, N. Neumann, and D. Plettemeier, "Analysis of substrate parameters' variations in a PCB-based 60 GHz GCPW Marchand balun design," in *Proc. 14th Eur. Conf. Antennas Propag. (EuCAP)*, Mar. 2020, pp. 1–5. [Online]. Available: https://ieeexplore.ieee.org/document/9135844/

[23] M. Umar, M. Laabs, N. Neumann, and D. Plettemeier, "Design of DC-blocks and bias-tee on PCB for V-Band," *IEEE Microw. Wireless Compon. Lett.*, vol. 31, no. 10, pp. 1107–1110, Oct. 2021. [Online]. Available: https://ieeexplore.ieee.org/document/9514580/

[24] M. Umar, M. Laabs, N. Neumann, and D. Plettemeier, "Bondwire model and compensation network for 60 GHz chip-to-PCB interconnects," *IEEE Antennas Wireless Propag. Lett.*, vol. 20, no. 11, pp. 2196–2200, Nov. 2021. [Online]. Available: https://ieeexplore.ieee.org/document/9525269/

[25] W. Fu, J. Hu, and S. Zhang, "Frequency-domain measurement of 60 GHz indoor channels: A measurement setup, literature data, and analysis," *IEEE Instrum. Meas. Mag.*, vol. 16, no. 2, pp. 34–40, Apr. 2013. [Online]. Available: http://ieeexplore.ieee.org/document/6495679/

[26] A. Ghosh and M. Kim, "THz channel sounding and modeling techniques: An overview," *IEEE Access*, vol. 11, pp. 17823–17856, 2023. [Online]. Available: https://ieeexplore.ieee.org/document/10047862/

[27] G. R. MacCartney and T. S. Rappaport, "A flexible millimeter-wave channel sounder with absolute timing," *IEEE J. Sel. Areas Commun.*, vol. 35, no. 6, pp. 1402–1418, Jun. 2017.

[28] C. Gentile et al., "Millimeter-wave channel measurement and modeling: A NIST perspective," *IEEE Commun. Mag.*, vol. 56, no. 12, pp. 30–37, Dec. 2018. [Online]. Available: https://ieeexplore.ieee.org/document/8570037/

[29] K. A. Remley, C. Gentile, A. Zajic, and J. T. Quimby, "Methods for channel sounder measurement verification," in *Proc. IEEE 86th Veh. Technol. Conf. (VTC-Fall)*, Sep. 2017, pp. 1–4. [Online]. Available: http://ieeexplore.ieee.org/document/8288374/

[30] T. Yucek and H. Arslan, "Time dispersion and delay spread estimation for adaptive OFDM systems," *IEEE Trans. Veh. Technol.*, vol. 57, no. 3, pp. 1715–1722, May 2008. [Online]. Available: http://ieeexplore.ieee.org/document/4357457/

[31] X. H. Mao, Y. H. Lee, and B. C. Ng, "Comparison of wideband channel sounding techniques," in *Proc. PIERS*, 2009, pp. 400–404.

[32] M.-T. Martinez-Ingles et al., "Channel sounding and indoor radio channel characteristics in the W-band," *EURASIP J. Wireless Commun. Netw.*, vol. 2016, no. 1, p. 30, Dec. 2016, doi: 10.1186/s13638-016-0530-7.

[33] Y. Lyu, P. Kyösti, and W. Fan, "Sub-THz VNA-based channel sounder structure and channel measurements at 100 and 300 GHz," in *Proc. IEEE 32nd Annu. Int. Symp. Pers., Indoor Mobile Radio Commun. (PIMRC)*, Sep. 2021, pp. 1–5. [Online]. Available: https://ieeexplore.ieee.org/document/9569702/

[34] S. Ranvier, M. Kyro, K. Haneda, T. Mustonen, C. Icheln, and P. Vainikainen, "VNA-based wideband 60 GHz MIMO channel sounder with 3-D arrays," in *Proc. IEEE Radio Wireless Symp.*, Jan. 2009, pp. 308–311. [Online]. Available: http://ieeexplore.ieee.org/document/4957340/

[35] P. F. M. Smulders and A. G. Wagemans, "Frequency-domain measurement of the millimeter wave indoor radio channel," *IEEE Trans. Instrum. Meas.*, vol. 44, no. 6, pp. 1017–1022, 1995. [Online]. Available: http://ieeexplore.ieee.org/document/475148/

[36] A. G. Siamarou and M. Al-Nuaimi, "A wideband frequency-domain channel-sounding system and delay-spread measurements at the license-free 57- to 64-GHz band," *IEEE Trans. Instrum. Meas.*, vol. 59, no. 3, pp. 519–526, Mar. 2010.

[37] L. Talbi and J. LeBel, "Broadband 60 GHz sounder for propagation channel measurements over short/medium distances," *IEEE Trans. Instrum. Meas.*, vol. 63, no. 2, pp. 343–351, Feb. 2014. [Online]. Available: http://ieeexplore.ieee.org/document/6601019/

[38] J. Luo, W. Keusgen, A. Kortke, and M. Peter, "A design concept for a 60 GHz wireless in-flight entertainment system," in *Proc. IEEE 68th Veh. Technol. Conf.*, Sep. 2008, pp. 1–5. [Online]. Available: http://ieeexplore.ieee.org/document/4657240/

[39] Infineon Technologies AG and ES Calif. *Single-Chip Packaged RF Transceivers for Mobile Backhaul*. Accessed: Jul. 25, 2022. [Online]. Available: https://www.microwavejournal.com/articles/20371-single-chip-packaged-RF-transceivers-for-mobile-backhaul

[40] Analog Devices. *HMC6000LP711E Millimeterwave Transmitter*. Accessed: Jan. 10, 2023. [Online]. Available: https://www.analog.com/media/en/technical-documentation/data-sheets/hmc6000.pdf

[41] Isola Group. (2023). *Isola I-Tera MT—Very Low-Loss Laminate and Prepreg*. [Online]. Available: https://www.isola-group.com/wp-content/uploads/data-sheets/i-tera-mt40.pdf

[42] E. Jorswieck and D. Plettemeier, "Massive MIMO ultra-efficient transmission," Commun. High-Freq. Technol., Technische Univ. Dresden, Deutsche Forschungsgemeinschaft (DFG), Bonn, Germany, Tech. Rep. 269256272, 2017. [Online]. Available: https://gepris.dfg.de/gepris/projekt/269256272

[43] M. Ortner, Z. Tong, and T. Ostermann, "A millimeter-wave wide-band transition from a differential microstrip to a rectangular waveguide for 60 GHz applications," in *Proc. 5th Eur. Conf. Antennas Propag. (EUCAP)*, Apr. 2011, pp. 1946–1949.

[44] Z. Tong, A. Stelzer, W. Menzel, C. Wagner, R. Feger, and E. Kolmhofer, "A wide band transition from waveguide to differential microstrip lines," in *Proc. Asia–Pacific Microw. Conf.*, Dec. 2008, pp. 1–4. [Online]. Available: http://ieeexplore.ieee.org/document/4957941/

[45] A. Ariffin and D. Isa, "Bandwidth enhancement of microstripline-to-waveguide transitions for broadband E-band module applications," *Microw. Opt. Technol. Lett.*, vol. 58, no. 6, pp. 1398–1401, Jun. 2016. [Online]. Available: https://onlinelibrary.wiley.com/doi/10.1002/mop.29836

[46] T. Yuasa, T. Oba, Y. Tahara, Y. Morimoto, T. Owada, and M. Miyazaki, "A millimeter wave wideband differential line to waveguide transition using short ended slot line," in *Proc. 44th Eur. Microw. Conf.*, Oct. 2014, pp. 1004–1007.

[47] B. Deutschmann and A. F. Jacob, "A full W-band waveguide-to-differential microstrip transition," in *IEEE MTT-S Int. Microw. Symp. Dig.*, Jun. 2019, pp. 335–338.

[48] Z. Tong and A. Stelzer, "A millimeter-wave transition from microstrip to waveguide using a differential microstrip antenna," in *Proc. 40th Eur. Microw. Conf.*, Sep. 2010, pp. 660–663.

[49] Z. Tong and A. Stelzer, "A vertical transition between rectangular waveguide and coupled microstrip lines," *IEEE Microw. Wireless Compon. Lett.*, vol. 22, no. 5, pp. 251–253, May 2012. [Online]. Available: http://ieeexplore.ieee.org/document/6185701/

[50] J. Shen, M. Aiken, C. Ladd, M. D. Dickey, and D. S. Ricketts, "A simple electroless plating solution for 3D printed microwave components," in *Proc. Asia–Pacific Microw. Conf. (APMC)*, Dec. 2016, pp. 1–4. [Online]. Available: http://ieeexplore.ieee.org/document/7931434/

[51] Analog Devices. (2023). *ADF4157—High Resolution 6 GHz Fractional-N Frequency Synthesizer*. [Online]. Available: https://www.analog.com/en/products/adf4157.html

[52] (2023). *CVCO55CW Series*. [Online]. Available: https://www.crystek.com/home/vco/cvcodetail.aspx?pn=CVCO55CW-1550-2500

[53] Redpitaya. *Red Pitaya—Swiss Army Knife for Engineers*. Accessed: Dec. 13, 2022. [Online]. Available: https://redpitaya.com/

[54] S. Salous, S. M. Feeney, X. Raimundo, and A. A. Cheema, "Wideband MIMO channel sounder for radio measurements in the 60 GHz band," *IEEE Trans. Wireless Commun.*, vol. 15, no. 4, pp. 2825–2832, Apr. 2016.